

Structural and electronic properties of bilayer epitaxial graphene

G. M. Rutter

School of Physics, Georgia Institute of Technology, Atlanta, Georgia 30332

J. N. Crain and N. P. Guisinger

Center for Nanoscale Science and Technology, NIST, Gaithersburg, Maryland 20899

P. N. First^{a),b)}

School of Physics, Georgia Institute of Technology, Atlanta, Georgia 30332

J. A. Stroscio^{a),c)}

Center for Nanoscale Science and Technology, NIST, Gaithersburg, Maryland 20899

(Received 8 October 2007; accepted 21 May 2008; published 1 July 2008)

Scanning tunneling microscopy and scanning tunneling spectroscopy (STS) are used to study the structural and electronic properties of bilayer epitaxial graphene on SiC(0001). Topographic images reveal that graphene conforms to the SiC interface morphology and is observed to be continuous across steps separating adjoining terraces. Bilayer epitaxial graphene is shown to be Bernal stacked as is evidenced by bias-dependent topographic imaging. STS maps of the differential conductance show that graphene lattice defects cause scattering of charge carriers near the Fermi level. An analysis of stationary scattering patterns observed in the conductance maps determines the energy-momentum dispersion relation within 100 meV of the Fermi level. In contrast to lattice defects, disorder at the SiC interface and at subsurface steps plays a much lesser role in the scattering of charge carriers. © 2008 American Vacuum Society. [DOI: 10.1116/1.2944257]

I. INTRODUCTION

Graphene, a two dimensional layer of sp^2 -bonded carbon atoms, has received much attention in the scientific community due to its unique mechanical and electronic properties.¹ These properties arise directly from graphene's lattice structure.^{2,3} The lattice is comprised of two equivalent carbon sublattices whose quantum state symmetries result in reduced backscattering of electrons and long coherence lengths.⁴ When a second graphene layer is added to form a bilayer, the sublattice symmetry is broken, resulting in variations in the electronic properties that depend on the stacking.⁵⁻⁷ One advantage of bilayer graphene is that a controllable energy gap can be induced by an electric field perpendicular to the layers.^{8,9} This induced gap, as well as inherent characteristics, makes bilayer graphene enticing for potential device applications.^{1,10,11} Magnetotransport characterization of graphene, which reveals many of its unique properties, has so far been performed on a few different forms of graphene: exfoliated graphene,¹ epitaxial graphene on Si-terminated SiC(0001),^{12,13} and epitaxial graphene on C-terminated SiC(000 $\bar{1}$).¹⁴ In this article, we consider epitaxial graphene grown on SiC(0001) substrates.

Epitaxial graphene on SiC offers a possible path for device applications and integration with mainstream electronics.^{1,12} Graphene can be grown in registry with the SiC substrate and patterned with well-established lithography procedures.^{12,14} Already, epitaxial graphene field effect devices have been demonstrated with gating from the top

side.¹³ The observed transport properties in any graphene device depend on the various defects, which can reduce the quantum state symmetries and lead to backscattering.¹⁵ A study of graphene defects and their effect on local electronic structure is therefore necessary to fully optimize future graphene devices. Scanning tunneling microscopy (STM) and scanning tunneling spectroscopy (STS) provide unique tools to investigate defect structure and perturbations of the local electronic structure near defect sites.^{16,17}

In this work, the structure and electronic properties of bilayer epitaxial graphene were studied via STM and STS at cryogenic temperature. Epitaxial graphene is found to follow the contours of the surface including the following: at a fine scale, the SiC $6\sqrt{3} \times 6\sqrt{3}R30^\circ$ interface reconstruction and, at larger scales, atomic steps separating adjoining terraces. Bias-dependent STM images of bilayer graphene are consistent with the Bernal *ABAB* stacking, as found in the most common form of graphite. To elaborate more on previous work,²² we show that lattice defects in graphene strongly scatter carriers near the Fermi level, leading to complex interference patterns in spatial maps of the differential conductance, dI/dV (a first order approximation of the local density of states of the sample). In contrast, disorder at the SiC interface and at subsurface steps plays a much lesser role in the scattering of charge carriers. An analysis of the interference patterns allows us to measure the energy-momentum relation for bilayer graphene near the Fermi level.

II. EXPERIMENT

Epitaxial graphene was grown on the silicon-terminated face of 4H-SiC(0001) in a graphitization process involving the thermal desorption of silicon at high annealing tempera-

^{a)} Author to whom correspondence should be addressed.

^{b)} Electronic mail: first@physics.gatech.edu

^{c)} Electronic mail: joseph.stroscio@nist.gov

tures. Before graphitization, samples were etched for 30 min under a flow of molecular hydrogen near atmospheric pressure at a temperature of 1550 °C. This process has been shown to remove polishing scratches that appear as nanometer deep gouges in atomic force microscopy images.¹⁸ The etching leaves an ordered SiC step array, with terraces for nominally on-axis SiC samples typically 0.4 μm in size and separated by 1 nm steps (the height of a 4H-SiC unit cell).¹⁸ The terrace size is determined by the miscut angle of the wafer. It is still unclear whether the initial quality of the SiC substrate substantially influences the graphene growth with regard to domain size¹⁹ and defect concentration.²⁰ After hydrogen etching, samples were graphitized by annealing to above 1200 °C in ultrahigh vacuum (UHV) using electron bombardment heating. The base pressure of the system was 1.33×10^{-8} Pa (1×10^{-10} Torr) with a maximum pressure of 4.6×10^{-6} Pa (3.5×10^{-8} Torr) during graphitization. The thickness of the graphene films was determined from an analysis of the ratio of silicon to carbon intensities obtained from *in situ* Auger electron spectroscopy measurements.²¹ The overall quality of the epitaxial graphene also was evaluated *in situ* by low energy electron diffraction. The data shown in what follows are from samples with an average graphene thickness of 2.5 layers. Epitaxial graphene samples were grown at the Georgia Institute of Technology and then transferred to the National Institute of Standards and Technology (NIST) for low-temperature STM measurements. After introduction into the UHV system at NIST, samples were outgassed at 800 °C for 5 min. Graphene samples and iridium probe tips, cleaned by field evaporation, were loaded into the cryogenic STM system. STM measurements were performed at constant tunneling currents after cooling to 4.2 K. Differential conductance, dI/dV , was measured with a lock-in amplifier, using a small voltage modulation, typically 0.4–1 mV, at a frequency of ≈ 500 Hz.

III. EPITAXIAL GRAPHENE

In order to understand the role of defects in the transport properties of epitaxial graphene, we present a detailed low-temperature STM study of defects found on these surfaces and their effect on the local electronic structure. Survey topographs reveal different structures that are large compared to the graphene lattice and occur commonly on this surface, as seen in Fig. 1. These structures are atomic steps [labeled A in Fig. 1(a)], tubular mounds [perhaps an early stage of carbon nanotube growth; labeled B in Fig. 1(a)], round mounds [labeled C in Fig. 1(b)], and the SiC interface reconstruction [seen as a small regular height modulation in the white box of Fig. 1(b)]. The B- and C-type mounds are rarely found on samples studied by room temperature STM after *in situ* graphene growth. We believe that they are a consequence of atmospheric exposure and subsequent UHV annealing. However, these structures cause little scattering of charge carriers. Strong scatterers of the electronic states are easily discernible in STM images from the appearance of a $\sqrt{3} \times \sqrt{3}R30^\circ$ pattern with respect to the graphene lattice,²² whereas no such patterns are observed in the vicinity of the aforementioned

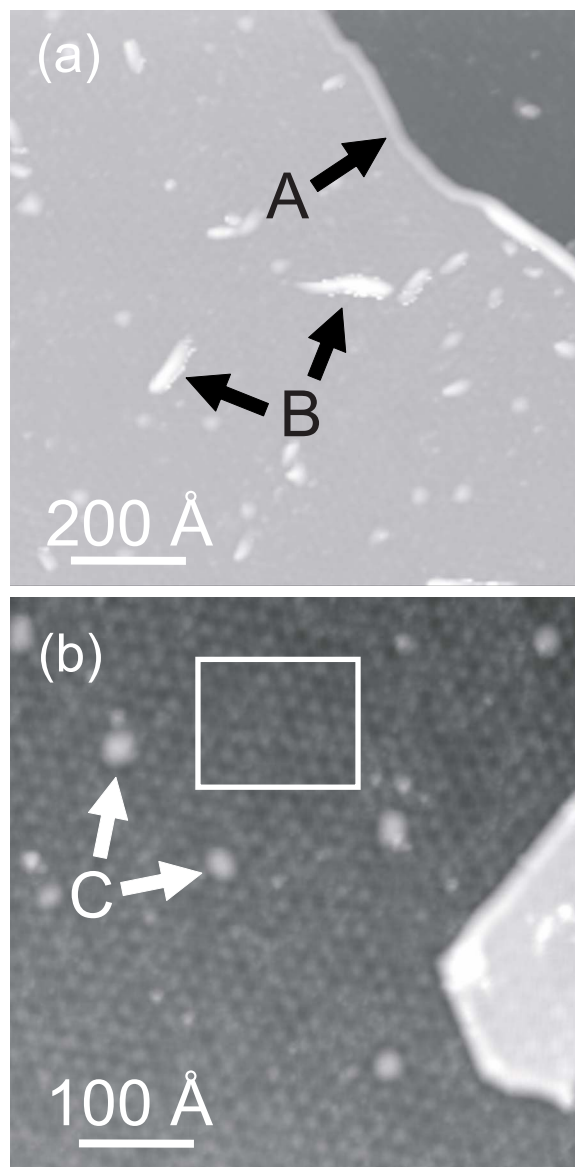


FIG. 1. Survey STM images display the different forms of extended features underneath bilayer epitaxial graphene on SiC. (a) $1000 \times 1000 \text{ \AA}^2$ STM topography at a tunneling bias and current of 0.4 V and 0.1 nA, respectively. Arrows are shown that indicate surface steps (labeled A) and tubular mounds (labeled B) that may be the initial formation of carbon nanotubes. (b) $500 \times 500 \text{ \AA}^2$ STM topography at a tunneling bias and current of 0.3 V and 0.1 nA, respectively. Indicated in this image are round mounds of possibly accumulated interface adatoms (labeled C) and the SiC interface reconstruction (height modulations seen in the white box).

structures. Apparently, these extended defects scatter only weakly because the graphene lattice remains continuous over subsurface protrusions.^{20,22,23} An example is shown in Fig. 2 for an atomic step edge separating single-layer and bilayer graphene.²⁴ The graphene lattice is clearly continuous over the step edge [Fig. 2(b)], though partially obscured in spots by interface states from the underlying SiC.²³ The continuous top layer implies a break in the graphene layer closest to the SiC interface. The blanketing nature of graphene is similar over steps in the SiC substrate. In cases where the graphene lattice terminates at a step edge (a geometry that can be

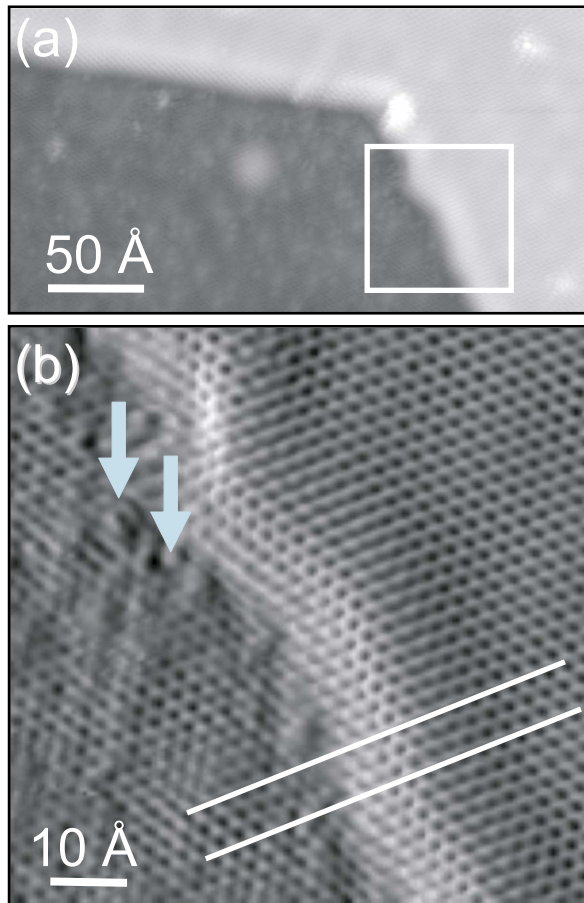


FIG. 2. Epitaxial graphene is shown to overlay surface steps, with little apparent scattering of electron states. (a) $300 \times 158 \text{ Å}^2$ STM topography at a tunneling bias and current of 0.3 V and 0.1 nA, respectively. This 3.1 Å step separates a region of single-layer and bilayer epitaxial graphene. (b) $75 \times 75 \text{ Å}^2$ derivative image that was cropped from (a) as indicated by the white box. As shown by the white lines, the topmost layer of graphene is essentially unperturbed by the step edge. Similar behavior is seen when epitaxial graphene overlays substrate SiC steps. The bumps that appear on the bottom terrace (blue arrows) are actually the transmission of the interface states through the single-layer graphene (Ref. 23).

created by tearing the layer during mechanical cleavage), strong scattering with a $\sqrt{3} \times \sqrt{3} R 30^\circ$ periodicity is seen.²⁵ We note the absence of $\sqrt{3} \times \sqrt{3} R 30^\circ$ patterns at epitaxial graphene step edges [Fig. 2(b)] due to the continuity of the graphene. Similar graphene continuity is observed over the tubular mounds found in the initial stages of graphene growth.²⁰

IV. BIAS-DEPENDENT IMAGING ON BILAYER GRAPHENE

Bias-dependent STM imaging identifies the stacking of epitaxial graphene bilayers as Bernal, found commonly in bulk graphite. Bias-dependent imaging is sensitive to spatial variations in the energy dependence of the local density of states for the two sublattices in graphene. Figures 3(a)–3(c) show three STM images from a bilayer terrace. At a sample bias of 0.1 V, the graphene lattice appears triangular [inset of Fig. 3(a)], indicating that only one of the two graphene sub-

lattices is imaged. Similar images have been observed in STM studies of bulk graphite²⁶ and multilayer graphene surfaces.^{22,27–30} An ideal graphene lattice, composed of the A and B sublattices, is displayed in the inset to help illustrate the atomic positions. As the sample bias is increased to 0.3 V [Fig. 3(b) and inset], STM images begin to show the second sublattice at a lower intensity. At an even higher tunneling bias of 0.4 V [Fig. 3(c) and inset], the images show a honeycomb structure similar to that observed for single-layer graphene, where both sublattices are imaged at almost the same intensity.^{23,27–30}

This bias-dependent imaging occurs when the sublattices of graphene (equivalent for a single layer) become distinguishable due to the stacking of the two graphene layers. In Bernal stacking, one sublattice of atoms in the top layer (A sublattice) is positioned directly over atoms in the bottom layer. However, atoms in the other top-layer sublattice (B sublattice) lie over hollow sites in the bottom layer, making the two sublattices inequivalent. This configuration results in a reduction in the low-energy density of states for the A sublattice as compared to the B sublattice, which suppresses the A sublattice imaging at low tunneling energies.^{31,32} At energies larger than the interlayer hopping energy, the two sublattices have essentially identical density of states. Since STM topography can be approximated as an integral over the density of states from 0 V (Fermi energy) to the applied bias voltage, the transition can be seen in the experimental data. The STM images show qualitative agreement with the theory: At low bias, the A sublattice density of states is suppressed, yielding images of only the B sublattice [Fig. 3(a)]. At higher bias, both sublattices image equivalently in the topography [Fig. 3(c)].

A more quantitative analysis can be made by measuring the apparent height difference between atoms on the A and B sublattices and comparing to estimates based on the theoretical local density of states.^{31,32} We use a simple tunneling model³³ and the sublattice densities of states calculated in Ref. 32 for bilayer graphene. From the Tersoff and Hamann model, the tunneling current is given approximately by $I_i \approx I_i^0 \exp(-2\kappa z_i)$ ($i=A, B$), where z_i is the tip-sample separation, and κ is the tunneling decay constant.³³ The dependence on the local density of states is through the tunneling integral $I_i^0 \propto \int_{E_F}^{eV_s} \rho_i(E) dE$, where E_F is the Fermi energy, eV_s is the sample bias multiplied by the electron charge, and $\rho_i(E)$ is the density of states on sublattice i .³³ The density of states can be broken into two energy regions: $|E| < \tau$, $\rho_A(E) < \rho_B(E)$ and $|E| > \tau$, $\rho_A(E) = \rho_B(E)$, where τ is the interlayer hopping energy.^{31,32} By setting $I_B = I_A$ for constant current imaging, we derive an expression for the difference in the apparent height on the two sublattices:

$$z_B - z_A = \frac{1}{2\kappa} \ln \left(\frac{\int_{E_F}^{eV_s} \rho_B(E) dE}{\int_{E_F}^{eV_s} \rho_A(E) dE} \right). \quad (1)$$

Figure 3(d) shows as black squares the measured values of $z_B - z_A$ from the topographs in Figs. 3(a)–3(c). Also included in the plot are relative heights at biases not shown in Figs. 3(a)–3(c) (blue circles). These data are taken on another area

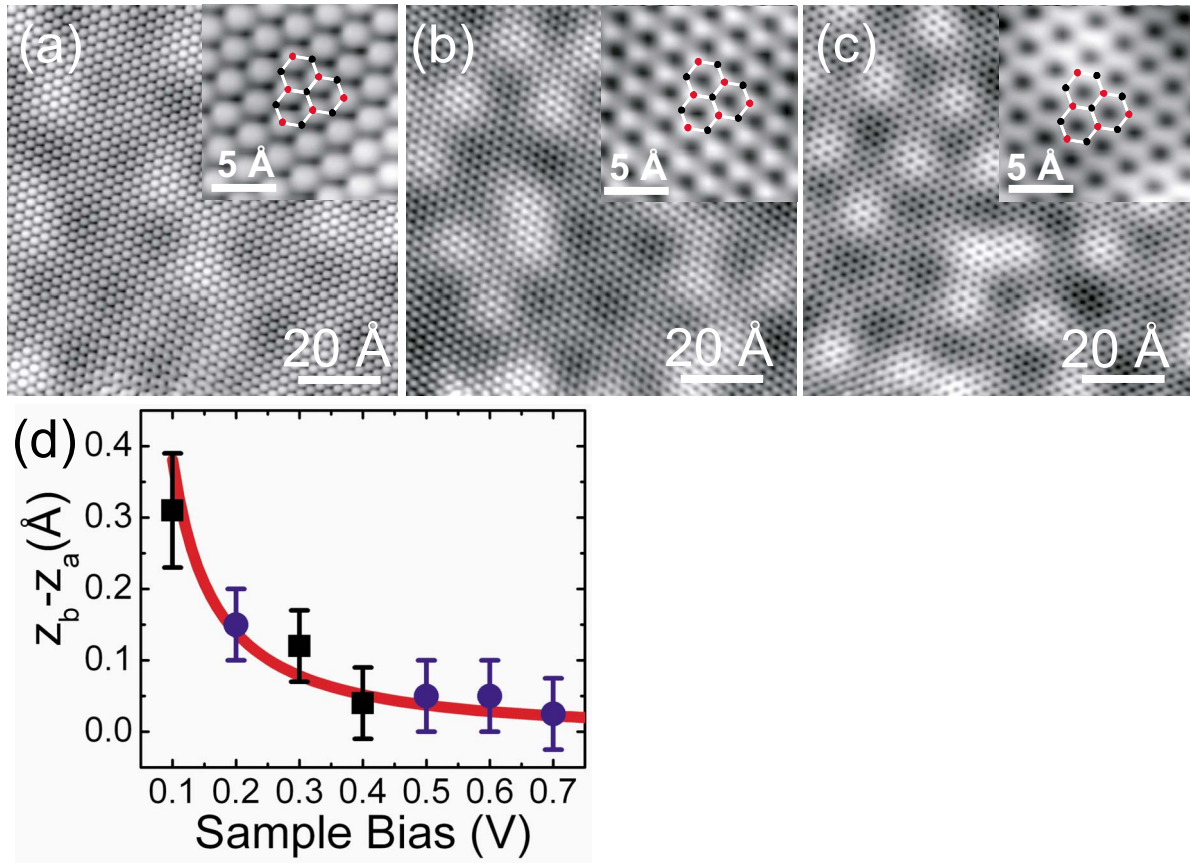


FIG. 3. STM measured apparent height differences between graphene basis atoms show Bernal stacking in bilayer graphene. [(a)–(c)] $95 \times 95 \text{ Å}^2$ STM topographs of the same area at a constant current of 0.1 nA and tunneling biases of (a) 0.1 V, (b) 0.3 V, and (c) 0.4 V. Insets in (a)–(c) are $15 \times 15 \text{ Å}^2$ cropped areas from the larger image, which give more insight into the atomic structure. A schematic of a graphene lattice, showing approximate atomic positions, is overlaid in each inset. Atoms on the B sublattice are shown in red and atoms on the A sublattice are shown in black. (d) Plot of the apparent height difference between atoms on the B and A sublattices. Experimental heights (black squares) were averaged from multiple line scans across several AB unit cells of the image. Additional data at other biases (blue circles) are measured from another area of the sample with a different probe tip. These relative heights are plotted alongside the data from Figs. 3(a)–3(c) for consistency and reproducibility. The data are compared to the calculated height difference (red line) obtained using independently measured parameters (see text).

of the sample with a different probe tip, which verifies the consistency and reproducibility of the analysis. The solid line in Fig. 3(d) is Eq. (1) with $2\kappa = 2 \text{ Å}^{-1}$,³³ $E_F = 0.3 \text{ eV}$,^{9,22} $\tau = 0.4 \text{ eV}$,^{32,34} and $\rho_l(E)$ from Ref. 32. Using this simple model, we find good agreement with experiment, which implies that the stacking order of the bilayer is Bernal and that the interlayer hopping energy $\tau \approx 0.4 \text{ eV}$. Although the data are not extensive, the agreement between experiment and theory is remarkable, using parameters that have been determined independently. We point out that the imaging transition can be tip dependent but is usually observed within the energy range shown in Fig. 3.

V. SCATTERING IN EPITAXIAL GRAPHENE

Differential conductance maps also yield a wealth of information about the electronic structure of bilayer graphene. Conductance maps are essentially energy-resolved pictures of the local density of states, with high spatial resolution. STS conductance maps on epitaxial graphene reveal that lattice defects scatter electrons very strongly, in comparison to subsurface defects.²² Figure 4 summarizes these results. Two

different varieties of graphene defects are observed in Fig. 4(a), one comprised of lattice defects and the other consisting of subsurface defects. Figure 4(b) shows a dI/dV map at -20 mV taken over the area of Fig. 4(a) at a tunneling bias and current of 0.1 V and 0.5 nA, respectively. Comparing the dI/dV map with the simultaneously acquired STM topography, it is clear that the lattice point defects, indicated by white arrows, cause the largest disturbances in the local density of states. Circular conductance maxima can be seen, centered at the point defect sites. These prominent features may be a consequence of nonlinear, and potentially ambipolar, screening in this low-density system. The superposition of electron waves scattered from the collection of such lattice defects creates a stationary interference pattern. The interference pattern shown in Fig. 4(b) has a long wavelength that is determined by intravalley scattering events that connect points at the same energy around the K_{\pm} points of the two dimensional Brillouin zone.²²

Higher resolution dI/dV maps reveal scattering with a short-wavelength modulation superimposed on the long-wavelength modulation, as shown in Fig. 4(d), with the cor-

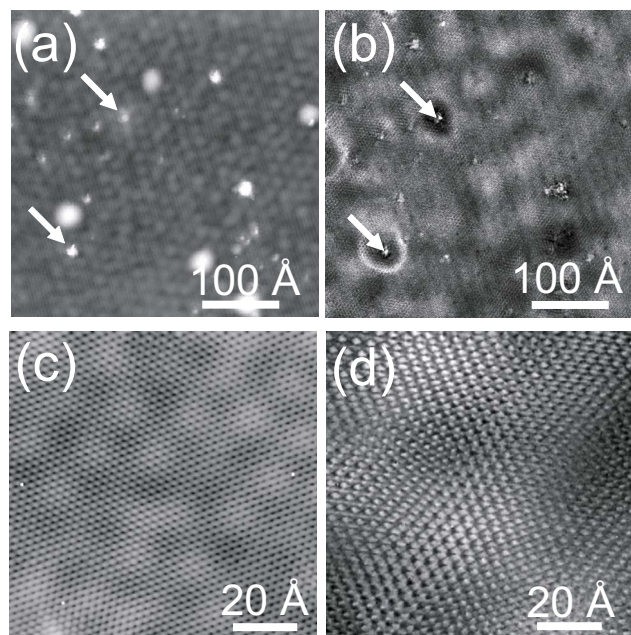


FIG. 4. Scattering in bilayer epitaxial graphene. (a) $400 \times 400 \text{ Å}^2$ STM topography displaying a variety of defects on the sample, taken at a tunneling bias and current of 0.1 V and 0.5 nA, respectively. (b) Simultaneously acquired differential conductance map at -20 mV , which shows that lattice defects (white arrows) cause the largest disturbance in the local density of states. A long-wavelength pattern also can be seen in the dI/dV maps and is attributed to intravalley scattering in the graphene. (c) $95 \times 95 \text{ Å}^2$ STM topography at a tunneling bias and current of 0.1 V and 0.5 nA, respectively. Simultaneously acquired differential conductance map at -5 mV , which shows a short-wavelength modulation imaged as well as the longer period. The interference pattern seen here is explained in terms of intervalley scattering in epitaxial graphene.

responding topography in Fig. 4(c). This short-wavelength modulation has been shown to arise from scattering between states on different constant energy contours from neighboring K_{\pm} points, often referred to as intervalley scattering.^{22,27} The scattering seen in Fig. 4(d) has a local $\sqrt{3} \times \sqrt{3}$ order with respect to the graphene unit cell, which is the same characteristic modulation period seen emanating from lattice defects in the topography.²² From measurements of the long and short wavelengths seen in the differential conductance maps, the local energy dispersion can be determined on a 10 nm length scale. The dispersion was found to be linear,²² with a slope (Fermi velocity $= 9.7 \times 10^5 \text{ m/s}$) and y intercept (Dirac point energy $= E_F - 330 \text{ meV}$) that are in agreement with transport¹² and photoelectron spectroscopy data for epitaxial graphene.^{9,35} Near the Dirac point, carrier wavelengths get bigger, requiring larger imaging areas and longer data acquisition times. Acquisition times are already quite long and approach instrumentation limits [$\approx 60 \text{ h}$ for the complete data set in Fig. 4(b)]. Future improvements to data acquisition rates will be required to explore this energy range.

VI. SUMMARY

We have presented detailed measurements of the surface atomic and electronic structure of bilayer epitaxial graphene,

obtained via STM and STS at cryogenic temperature. STM imaging shows that epitaxial graphene follows the surface contours of the underlying SiC interface. Bias-dependent images determine that bilayer graphene is Bernal (*AB*) stacked. Despite this Bernal stacking, bilayer graphene shows linear band dispersion within 100 meV of the Fermi energy. Scattering from extended defects beneath the graphene surface is limited, while scattering from lattice defects causes the largest perturbations of the local density of states. The suppression of intra- and intervalley scatterings is one of the hallmarks of graphene, leading to long coherence lengths. This work shows that lattice defects break the local symmetry and cause enhanced backscattering. Future work must address fabrication methods and seek further correlations between atomic scale measurements and observed transport properties.

ACKNOWLEDGMENTS

The authors thank Mark Stiles, Walt de Heer, Claire Berger, and Francisco Guinea for valuable comments and discussions and Steven Blankenship, Frank Hess, Alan Band, Nate Brown, and Tianbo Li for their technical assistance. One author (N.P.G.) acknowledges a National Research Council Postdoctoral Fellowship. This work was supported in part by the Office of Naval Research, by Intel Research, and by NSF Grant Nos. ECCS-0404084 and ECCS-0521041.

- ¹For a review, see, e.g., A. K. Geim and K. S. Novoselov, *Nat. Mater.* **6**, 183 (2007).
- ²P. R. Wallace, *Phys. Rev.* **71**, 622 (1947).
- ³J. C. Slonczewski and P. R. Weiss, *Phys. Rev.* **109**, 272 (1958).
- ⁴T. Ando, T. Nakanishi, and R. Saito, *J. Phys. Soc. Jpn.* **67**, 2857 (1998).
- ⁵E. McCann and V. I. Fal'ko, *Phys. Rev. Lett.* **96**, 086805 (2006).
- ⁶K. S. Novoselov *et al.*, *Nat. Phys.* **2**, 177 (2006).
- ⁷J. M. B. Lopes dos Santos, N. M. R. Peres, and A. H. Castro Neto, *Phys. Rev. Lett.* **99**, 256802 (2007).
- ⁸E. McCann, *Phys. Rev. B* **74**, 161403(R) (2006).
- ⁹T. Ohta, A. Bostwick, T. Seyller, K. Horn, and E. Rotenberg, *Science* **313**, 951 (2006).
- ¹⁰M. I. Katsnelson, *Mater. Today* **10**, 20 (2006).
- ¹¹H. Min, G. Borghi, M. Polini, and A. H. MacDonald, *Phys. Rev. B* **77**, 041407(R) (2008).
- ¹²C. Berger *et al.*, *J. Phys. Chem. B* **108**, 19912 (2004).
- ¹³G. Gu, S. Nie, R. M. Feenstra, R. P. Devaty, W. J. Choyke, W. K. Chan, and M. G. Kane, *Appl. Phys. Lett.* **90**, 253507 (2007).
- ¹⁴C. Berger *et al.*, *Science* **312**, 1191 (2006).
- ¹⁵J. H. Chen, C. Jang, M. S. Fuhrer, E. D. Williams, and M. Ishigami, *Nat. Phys.* **4**, 377 (2008).
- ¹⁶H. A. Mizes and J. S. Foster, *Science* **244**, 559 (1989).
- ¹⁷M. F. Crommie, C. P. Lutz, and D. M. Eigler, *Nature (London)* **363**, 524 (1993).
- ¹⁸P. Martensson, F. Owman, and L. I. Johansson, *Phys. Status Solidi B* **202**, 501 (1997).
- ¹⁹J. Hass *et al.*, *Appl. Phys. Lett.* **89**, 143106 (2006).
- ²⁰N. P. Guisinger, G. M. Rutter, J. N. Crain, C. Heiliger, P. N. First, and J. A. Stroscio, *J. Vac. Sci. Technol. A* (to be published).
- ²¹For a review, see, e.g., W. A. de Heer *et al.*, *Solid State Commun.* **143**, 92 (2007).
- ²²G. M. Rutter, J. N. Crain, N. P. Guisinger, T. Li, P. N. First, and J. A. Stroscio, *Science* **317**, 219 (2007).
- ²³G. M. Rutter, J. N. Crain, N. P. Guisinger, T. Li, P. N. First, and J. A. Stroscio, *Phys. Rev. B* **76**, 235416 (2007).
- ²⁴Bilayer graphene has been shown to be distinguishable from single-layer graphene by a reduction in the STM imaging of SiC interface states as described in Ref. 23.

- ²⁵P. L. Giunta and S. P. Kelty, J. Chem. Phys. **114**, 1807 (2001).
- ²⁶D. Tomanek, S. G. Louie, H. J. Mamin, D. W. Abraham, R. E. Thomson, E. Ganz, and J. Clarke, Phys. Rev. B **35**, 7790 (1987).
- ²⁷P. Mallet, F. Varchon, C. Naud, L. Magaud, C. Berger, and J. Y. Veuillen, Phys. Rev. B **76**, 041403(R) (2007).
- ²⁸V. W. Brar *et al.*, Appl. Phys. Lett. **91**, 122102 (2007).
- ²⁹E. Stolyarova *et al.*, Proc. Natl. Acad. Sci. U.S.A. **104**, 9209 (2007).
- ³⁰M. Ishigami, J. H. Chen, W. G. Cullen, M. S. Fuhrer, and E. D. Williams, Nano Lett. **7**, 1643 (2007).
- ³¹J. Nilsson, A. H. C. Neto, F. Guinea, and N. M. R. Peres, Phys. Rev. Lett. **97**, 266801 (2006).
- ³²Z. F. Wang, Q. X. Li, H. B. Su, X. P. Wang, Q. W. Shi, J. Chen, J. L. Yang, and J. G. Hou, Phys. Rev. B **75**, 085424 (2007).
- ³³J. Tersoff and D. R. Hamann, Phys. Rev. B **31**, 805 (1985).
- ³⁴F. Guinea, A. H. Castro, and N. M. R. Peres, Solid State Commun. **143**, 116 (2007).
- ³⁵S. Y. Zhou *et al.*, Nat. Mater. **6**, 770 (2007).